Brief Communication: Sensitivity of Antarctic ice-shelf melting to ocean warming across basal melt models

Erwin Lambert[1*] and Clara Burgard[2,3*]

[1]Royal Netherlands Meteorological Institute (KNMI), Utrechtseweg 297, 3731 GA, De Bilt, The Netherlands
[2]Laboratoire d'Océanographie et du Climat: Expériences et Approches Numériques (LOCEAN), Sorbonne Université, CNRS/IRD/MNHN, Paris, France
[3]IGE, Univ. Grenoble Alpes, IRD/CNRS/INRAE/Grenoble INP, Grenoble, France
[*]These authors contributed equally to this work.

Correspondence: Erwin Lambert (erwin.lambert@knmi.nl)

Abstract. The uncertain sensitivity of Antarctic ice-shelf basal melt to ocean warming strongly contributes to uncertainties in sea-level projections. Here, we explore the response of five dedicated basal melt models to an idealised sub-thermocline 1 °C warming and find a large intermodel spread with total melt increases between 67% and 240%. For deep regions of presently fast-melting ice shelves, this spread can reach two orders of magnitude. We conclude that a consistent calibration on present-day conditions does not guarantee consistent melt sensitivities and that diversity in basal melt forcing is presently unavoidable to prevent underestimating uncertainties in future projections.

1 Introduction

The Antarctic Ice Sheet loses mass at an accelerating rate, leading to an increasing contribution to sea-level rise (Otosaka et al., 2023). This mass loss is mainly driven by ocean-induced melting at the base of Antarctic ice shelves (most recent estimates by Davison et al., 2023), leading to ice-shelf thinning, reduced buttressing and a consequential increase in the flux from the grounded ice toward the ocean. The future evolution of ocean-induced ice-shelf melt therefore plays a crucial role in projections of the Antarctic Ice Sheet evolution and its contribution to sea-level rise.

Ocean-induced ice-shelf melt, here referred to as basal melt, is best simulated in a coupled ocean–ice-sheet framework, where the ocean circulation in the cavities below the ice shelves is resolved and the ice-sheet geometry responds to the melt occurring at the ice-ocean interface. However, coupled ocean–ice-sheet models currently remain rare and too expensive to run circum-Antarctic or global simulations at sufficiently high resolution over centennial to millenial time scales.

Instead, ice-sheet modelers rely on simpler models to provide basal melt forcing to Antarctic ice-sheet models (e.g. Jourdain et al., 2020). In recent decades, a variety of such dedicated basal melt models has been developed, ranging from simple parameterisations, assuming a linear or quadratic dependency on the difference between the ocean temperature and local freezing point (e.g. Jourdain et al., 2020), to simple models emulating the circulation in the cavity assuming plume dynamics (e.g. Lazeroms et al., 2018), an overturning circulation (Reese et al., 2018), or both (Pelle et al., 2019), to more complex models

resolving the horizontal circulation component (Lambert et al., 2023) or relying on machine learning techniques (e.g. Burgard et al., 2023).

For their initial development, all basal melt models were calibrated and assessed on present-day observations or simulations close to present-day conditions and thus applied to force numerous ice-sheet models. However, the evaluation of a subset of models against a common reference revealed a large spread in the resulting melt rates and melt patterns (Burgard et al., 2022, 2023). An idealised ice-sheet modeling study also revealed the choice of basal melt model to dominate the uncertainty in mass loss and grounding line retreat (Berends et al., 2023). In addition, the application of several models on ocean properties simulated by a coupled ocean–ice-sheet model showed large discrepancies in the melt resulting from ocean conditions warmer than present (Burgard et al., 2023), raising the question how the basal melt models differ in terms of their sensitivity to ocean warming.

To assess the intermodel spread in basal melt sensitivity to ocean warming, we here compare a subset of five dedicated basal melt models of different levels of complexity. First, we calibrate the basal melt models based on an idealised ocean forcing mimicking present-day conditions and on satellite-derived estimates of present-day melt. Second, we apply an ocean forcing representing a sub-thermocline 1 °C warming and quantify the change in melt rates and melt patterns. With this study, we highlight and interpret key differences in the behaviour of the various basal melt models for present-day and warm ocean conditions and provide an intermodel range of basal melt sensitivities for the 40 largest Antarctic ice shelves. As no observational dataset is available to evaluate the sensitivities, we cannot provide a recommendation of the best or worst performing model. Instead, we aim to provide users with an overview of the behaviour of the different basal melt models in terms of patterns and sensitivity to ocean warming.

2 Data and Methods

To simulate a basal melt pattern, each model requires information on ice shelf cavity geometries as well as an ocean forcing in the form of a vertical profile of temperature and salinity in front of each ice shelf. In the following, we describe the input data (Sec. 2.1), the five basal melt models (Sec. 2.2), the experimental setup (Sec. 2.3), and our calibration approach for the free parameters (Sec. 2.4).

2.1 Data

The ice-shelf geometries are based on the most recent version of the BedMachine dataset (BedMachine v3, Morlighem et al., 2020), which we regrid to a 2x2 km horizontal grid. We define the ice shelf domains based on masks from the Ice sheet Mass Balance Intercomparison Exercise (IMBIE) community (Rignot et al., 2019). In order to allow the representation of meltwater exchange within shared cavities of neighbouring ice shelves, we merge ice shelves that have no clear distinction from an oceanic point of view (such as e.g. Filchner–Ronne and Crosson–Dotson) into one. Throughout this study, we focus on the 40 largest ice shelves of the remaining ensemble, containing all ice shelves with an area of at least 1000 km^2.

The observational estimates of basal melt used for the present-day calibration are taken from Paolo et al. (2023). These are based on 26 years (1992–2017) of satellite altimetry. For calibration, we use the melt rates averaged over the whole period.

2.2 Basal melt models

We compare the behaviour of five basal melt models: the Quadratic parameterisation, the PICO model, the Plume model, the 2D model LADDIE, and a Neural Network.

- In the Quadratic parameterisation (e.g. Jourdain et al., 2020), basal melting is expressed as a quadratic function of the difference between the local ocean temperature, directly extrapolated from the temperature in front of the ice shelf, and the local freezing point. Here, we adopt the quadratic-local formulation accounting for the local ice-shelf slope as described by Burgard et al. (2022).

- PICO (Reese et al., 2018) is a box model that mimics an overturning circulation in the cavity. Only the bottom ocean properties in front of the ice shelf are applied at the grounding line and then modified while being advected along the ice-shelf draft, across a number of boxes dependent on the distance from the grounding line, leading to melting and freezing along the way.

- The Plume model (e.g. Lazeroms et al., 2018) is a one-dimensional model of a buoyant meltwater plume formed at the grounding line and rising along the ice-shelf draft following prescribed flowlines on the two-dimensional grid. We use the implementation by e.g. Burgard et al. (2022) but include an improved method to identify the origin grounding line depth by propagating plume paths from the grounding line to the rest of the ice shelf.

- The two-dimensional model LADDIE (Lambert et al., 2023) solves the vertically integrated Navier-Stokes equations in the upper mixed layer of the ice shelf cavity. Melt rates are computed using the commonly adopted "three-equations parameterisation" and the overturning is represented by a parameterised entrainment. The model can be seen as an extension of the one-dimensional Plume model, accounting for the horizontal flow under influence of geometric steering and Coriolis deflection.

- The Neural Network (Burgard et al., 2023) is a simple multilayer perceptron trained to emulate a cavity-resolving version of the ocean model NEMO at 1/4°horizontal resolution (more details about these simulations in Burgard et al., 2022). Compared to Burgard et al. (2023), the training dataset has been expanded with several projections, including those from Mathiot and Jourdain (2023), to account for warmer ocean conditions.

2.3 Experiments

For each model and ice shelf, two experiments are performed: a reference (REF) and a warm (WARM) experiment. The REF experiment is designed to represent present-day conditions in an idealised framework. Ocean conditions are divided into six categories (Fig. 1a): Bellingshausen, East-Amundsen, West-Amundsen, Cool, Cold, and HSSW (i.e. High Salinity Shelf

Water). The first four contain a thermocline separating an upper layer at surface freezing temperature from a warm layer of Circumpolar Deep Water (CDW). The thermocline depth is taken at 500 m (similar to observations in the Amundsen Sea as in
85 e.g., Dutrieux et al., 2014) except for the Bellingshausen Sea where a shallower thermocline exists; there, a depth of 380 m is taken.

The warm water mass has a temperature of 1.2 °C (Bellingshausen and East-Amundsen), 0.4 °C (West-Amundsen), and -1.2 °C (Cool). These values are inspired by in-situ observations (e.g., Dutrieux et al., 2014) where possible. The Cold ocean conditions are described by a full water column at surface freezing point. Finally, the HSSW conditions contain a linear
90 function of temperature of -0.3 °C per 1000 m to represent the presence of High Salinity Shelf Water, producing a temperature of approximately -2.1 °C at 1000 m, comparable to observations in the Filchner trough (Sallée et al., 2023). Salinities are taken such that a quadratic density stratification arises, again inspired by in-situ observations, except for HSSW, where a linear stratification is imposed.

Several experimental choices, such as the exact values of the Bellingshausen thermocline depth, the Cool sub-thermocline
95 temperature, and the division of ice shelves with Cold and Cool forcing, cannot be sufficiently constrained by observations. In that case, we apply a form of inversion in which we optimise the REF forcing using LADDIE to reproduce observed basal melt rates in the associated regions. As a consequence, the agreement between simulated melt rates by LADDIE and observational melt estimates may be slightly exaggerated in comparison to the other four models.

For each ice shelf, we prevent CDW from intruding into the cavity if there is a bathymetric obstacle at the ice-shelf front. For
100 points within the cavity that are deeper than this bathymetric obstacle, temperature and salinity are extrapolated downwards. from the deepest entrance depth.

For the WARM experiment, we add 1 °C to the temperature below 500 m, which is the depth of our idealised CDW in most regions, and we leave the upper layer unchanged. A salinity anomaly is applied to compensate for the temperature anomaly, such that the density profile is identical for REF and WARM experiments.

105 We extract two melt sensitivities based on the REF and WARM experiments. The linear sensitivity equals the difference in melt rates (WARM-REF) divided by the increase in the temperature forcing at the deepest point of the ice shelf. If unblocked by bathymetric obstacles, this temperature increase is 1 °C. If blocked, this temperature increase is between 0 and 1 °C (Fig. 1a). The quadratic sensitivity is derived from a quadratic fit through the melt rates from these two experiments, complemented by a third data point of zero melt and a temperature forcing equal to the local freezing temperature. As changes in basal melt in the
110 deep regions of ice shelves may have a larger impact than changes in shallower regions and melt sensitivities in deep regions may be considerably higher than ice-shelf averages (e.g., Jourdain et al., 2020), we additionally define the 'deep amplification'. This nondimensional metric quantifies the ratio between the melt rate or melt sensitivity in the deepest 10% of an ice shelf and the ice-shelf average. A deep amplification of 2 indicates that either the melt rate or the melt rate sensitivity in the deepest 10% is a factor 2 higher than the ice-shelf average.

2.4   Calibration

To enable a consistent intercomparison between the different basal melt models, we calibrate them on the same reference state, which mimicks present-day conditions. We use the temperature and salinity profiles from the REF experiment as forcing and calibrate the models to minimise the absolute difference to the observed ice-shelf melt (Paolo et al., 2023) averaged over the 40 ice shelves (0.60 m yr^{-1}). For the Quadratic parameterisation, this leads to a turbulent exchange coefficient parameter K of 7.8×10^{-5}.

Both PICO and the Plume model have two tuning parameters and trial and error indicates that the empirical functions between the parameters derived by Burgard et al. (2022) cause an underestimation of the melt. Instead, for PICO, we take the effective turbulent temperature exchange velocity $\gamma_T^\star$ leading to the maximum melt using the empirical function and then infer the corresponding overturning coefficient C needed to reach the target melt, resulting in $\gamma_T^\star$=0.85×10^{-5} and C=7.4×10^{6}. For the Plume model, we probe the plausible parameter space (shown in Fig. 9a of Burgard et al., 2022) and find a minimum absolute difference for a Stanton number of 3.2×10^{-4} and an entrainment coefficient E_0 of 11.9×10^{-2}.

As the REF profiles were partly designed based on an inversion-like method with LADDIE, no recalibration of LADDIE is needed. The main tuning parameters are the top drag coefficient $C_{d,top} = 1.1$ and the minimum layer thickness $D_{min} = 6.6m$ (Lambert et al., 2023). For the Neural Network, the 40 data points are insufficient for a robust new training. Hence, we use the version where training has been extended to projections and use it as a NEMO emulator, accepting potential biases in the reference state.

3   Results and discussion

3.1   Reference melt patterns

Overall, the consistent calibration on the circum-Antarctic ice-shelf melt yields similar average melt rates, between 0.58 and 0.60 m yr^{-1}, for four out of five basal melt models (Fig. 1c-f). The Neural Network, which could not be recalibrated, produces slightly lower average melt rates of 0.45 m yr^{-1} (Fig. 1g), which is likely the consequence of a warm bias in the training dataset. In addition to average melt rates, all basal melt models reproduce the comparably higher melt rates for the ice shelves in the Amundsen Sea and Totten/Moscow University ice shelves. This illustrates that the contrast between warm and cold ocean conditions is appropriately translated to a contrast between high and low melt rates by all models. A comparison of the melt rates between Amundsen Sea (observed: O(10 m yr^{-1})) and Filchner–Ronne (observed: O(0.1 m yr^{-1})) reveals that this contrast is underestimated by an order of magnitude by the Plume model and the Neural Network (O(5 m yr^{-1}) vs O(0.5 m yr^{-1})).

In terms of patterns of melting and freezing, the Quadratic parameterisation stands out in several ways (Fig. 1c). First, the patterns are purely governed by the depth of the ice shelf draft and by the local slope. Second, the model does not reproduce refreezing as this requires a representation of advection of meltwater. The purely depth-dependent pattern and explicit slope-
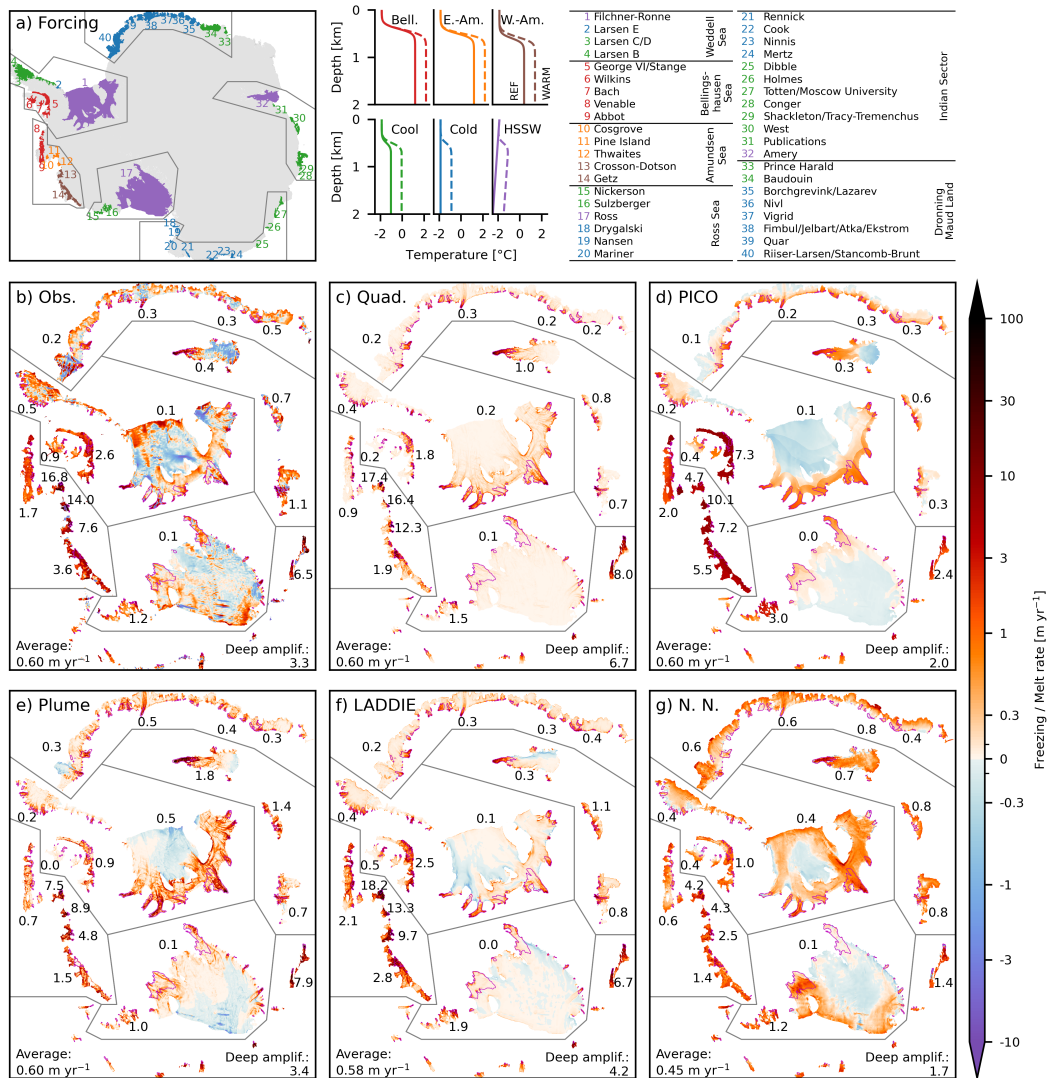
Figure 1. Ocean forcing and reference basal melt patterns. (a) Forcing, denoted by six colours, applied to 40 major ice shelves, and corresponding ice-shelf names. Temperature profiles denote REF (solid) and WARM (dashed) forcing. The map also displays the contours of the 'puzzle pieces' shown in panels (b) to (g). Basal melt patterns [m yr^{-1}] for (b) present-day observational estimates (Paolo et al., 2023) and (c) the Quadratic parameterisation, (d) PICO, (e) the Plume model, (f) LADDIE, and (g) the Neural Network (N.N.), forced with REF forcing. The numbers shown along a selection of ice shelves are average melt rates in m yr^{-1}. The spatial average over the 40 ice shelves is shown in the bottom left; the melt amplification in the deepest 10% of each ice shelf (marked by magenta lines) is shown in the bottom right.

dependence combine into a strong deep amplification. For the Quadratic parameterisation, this value (6.7) is twice the value derived from observations (3.3).

The spatial patterns of PICO are strongly constrained by the box pattern (Fig. 1d). The inherent assumption of highest melt in the first box closest to the grounding line leads to wide bands of relatively uniform melting along the grounding lines and,

150 in the case of cold cavities, relatively uniform refreezing in the center and close to the ice shelf fronts. As the melt rates are by design weakly dependent on depth and independent from the draft slope, the deep amplification is relatively low (2.0) compared to observations.

The melt patterns of the Plume model (Fig. 1e) display a stronger heterogeneity than the Quadratic and PICO models. In this model, the local slope angle relative to the imposed meltwater pathway induces small-scale variations in melting and refreezing.

155 Similar to PICO, the transition from melting to refreezing in the cold ice shelves occurs further away from the grounding line than in the observations. However, the deep amplification is nearly identical to the observed value, indicating that the depth- and slope-dependence of melt rates are well represented by this model.

In comparison to the prescribed meltwater flowlines in the Plume model, the resolved meltwater circulation by LADDIE (Fig. 1f) allows for a number of additional features. In particular, the impact of Coriolis deflection leads to an asymmetry in

160 melting and refreezing rates which are concentrated near the Western boundaries, in qualitative agreement with the observed patterns. In addition, the resolved circulation leads to a better positioning of the transition from melting to refreezing, closer to the grounding line, than PICO and the Plume model. The deep amplification (4.2) is higher than observed, possibly related to the imposed minimum layer thickness, which can lead to an overestimation of the heat transport to the deepest grounding lines.

165 The melting and freezing patterns simulated by the Neural Network (Fig. 1g) also reflect the Coriolis-deflected meltwater circulation as simulated by NEMO. This allows for a generally well-distributed pattern of melting and refreezing on the Filchner–Ronne and Ross ice shelves. In addition, the Neural Network simulates 'mode 3' melting close to the ice shelf front, most visible along Dronning Maud Land and the Filchner–Ronne and Ross ice shelves. This melting is caused by the presence of Antarctic Summer Water (AASW), and cannot be explained by our forcing (hence this melting is not simulated by the other

170 models). Instead, it is an intrinsic feature learned from the NEMO training dataset that the Neural Network will reproduce regardless of the applied forcing. The Neural Network shows the lowest deep amplification, which is a reflection of lower melting at depth in NEMO due to a lower resolution and therefore a smoother and shallower ice draft.

3.2 Melt sensitivity

All ice shelves show an increase in basal melting in response to a sub-thermocline ocean warming by 1 °C (Fig. 2), ranging

175 from 67% for the Neural Network to 240% for the Quadratic parameterisation, with a median of 175%. In all models, the melt sensitivity is strongest at depth, reflected by values of the deep amplification above 1, ranging from 1.7 (PICO) to 5.5 (Quadratic). Combining the average melt rate and deep amplification, this translates to a spread in the melt response in the deepest 10% of the ice shelves ranging from 0.8 (Neural Network) to 7.9 m yr^{-1} (Quadratic).

The patterns of the melt response show distinct features related to the underlying model assumptions. The Quadratic pa-

180 rameterisation shows zero melt increase in the shallowest regions as it does not account for advection from the deeper regions where warming is applied. PICO shows a relatively uniform melt response which is strongly constrained by the box structure.
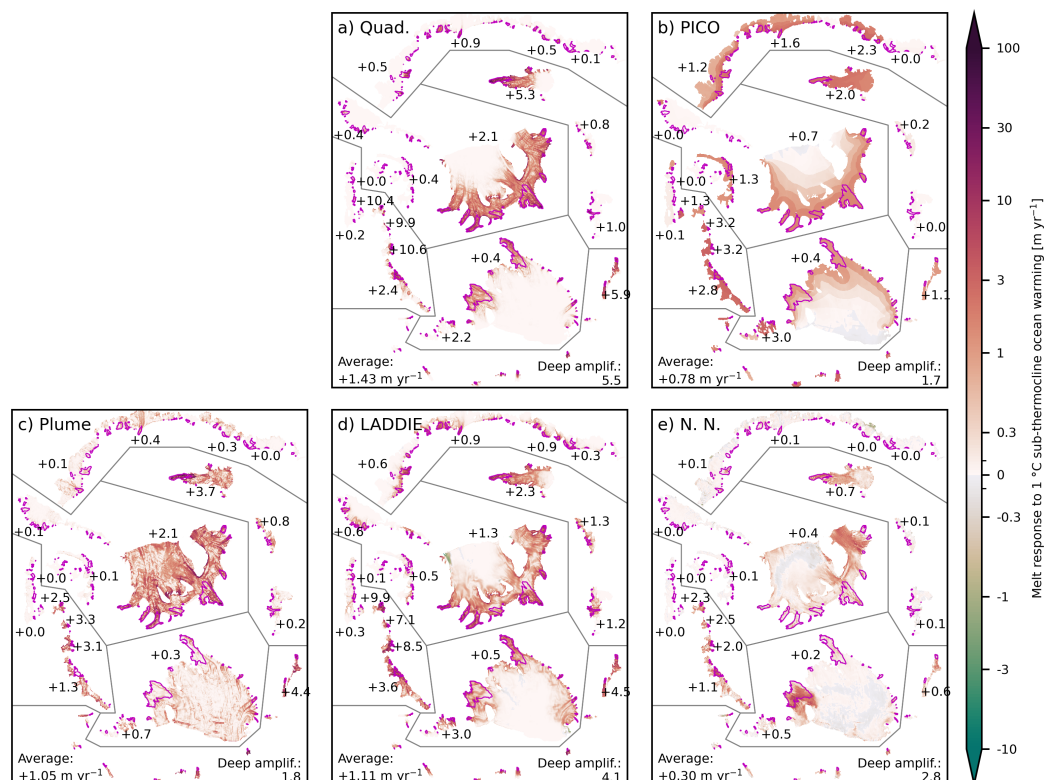
7

Figure 2. Spatial melt response to a 1 °C sub-thermocline warming expressed as the increase in melt relative to the reference (shown in Fig. 1) for the (a) the Quadratic parameterisation, (b) PICO, (c) the Plume model, (d) LADDIE, and (e) the Neural Network (N.N.). The numbers indicate the average response for selected ice shelves. The numbers at the bottom denote the Antarctic-wide average response (left) and the Antarctic-wide deep amplification of the melt response (right; determined in the deepest 10% of each ice shelf as denoted by the magenta lines).

The Plume shows a scattered melt response, mainly driven by the local slopes. LADDIE shows melt patterns reflecting the advective pathway of the simulated meltwater plumes. The Neural Network shows a melt response concentrated in specific regions, possibly reflecting a sensitivity in the cavity circulation in NEMO.

185 The melt sensitivities according to the different models can vary by an order of magnitude (Fig. 3a,c). The lowest values are produced by the Neural Network, whereas the Quadratic parameterisation and LADDIE produce on average the strongest sensitivities. In the case of the linear sensitivities (Fig. 3a), both average and median values of all models fall below the uncertainty ranges of previous estimates of bulk sensitivities from LARMIP-2 (Levermann et al., 2020) and from van der Linden et al. (2023). By design, the quadratic sensitivities are better constrained. This leads to a smaller intermodel spread

190 (Fig. 3c) and a somewhat better agreement with previous assessments from ISMIP6 (Jourdain et al., 2020) and van der Linden et al. (2023). Despite the strong intermodel disagreement, however, all models agree that with the current calibration method the Antarctic-wide melt sensitivities are markedly lower than these previous estimates.
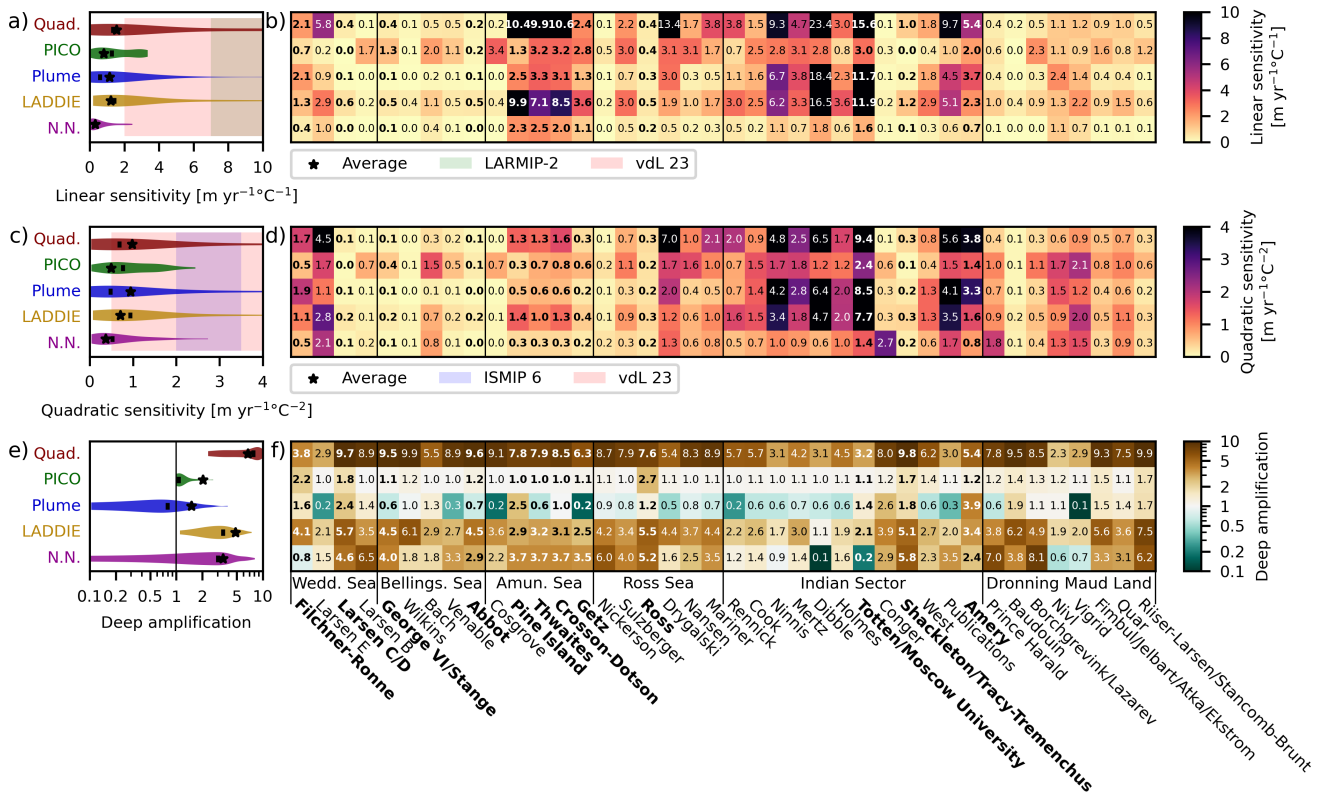
8

Figure 3. Melt sensitivity indicator distributions and values per ice shelf for each model. (a) Linear and (c) quadratic melt sensitivity distribution of all 40 ice shelves (unweighted). The star denotes the area-weighted mean and the vertical line is the median. Background shading are reference values from the literature: LARMIP-2 (full range, Levermann et al., 2020), vdL 23 (5–95%, van der Linden et al., 2023) and ISMIP6 (5–95%, Jourdain et al., 2020). (b) Linear and (d) quadratic melt sensitivity of each individual ice shelf. (e) Deep amplification of the melt response (ratio deepest 10% versus ice shelf average) distribution across ice shelves and (f) values for each individual ice shelf. The value 1 indicates no deep amplification. The bold-faced names are the major ice shelves mentioned in the text.

On the individual ice-shelf level, some consensus on the melt sensitivity is found between the models, despite the overall strong intermodel disagreement. All models agree on a general classification of the major ice shelves, denoted by bold-faced names in Fig. 3, into three consensual categories: those with comparably weak, moderate, or strong melt sensitivities. For the Shackleton/Tracy Tremenchus, Ross, Abbot, George VI/Stange, and Larsen C/D ice shelves, all models produce a weak sensitivity of the ice-shelf average melt. This consensus is best reflected by the quadratic sensitivities (Fig. 3c) with values (well) below 0.5 m yr^{-1} °C^{-2}. In addition, all models agree to some extent on a moderate sensitivity for Amery, Getz, and Filchner–Ronne. For Filchner–Ronne specifically, the linear melt sensitivity of LADDIE (1.3 m yr^{-1} °C^{-1}) is closest to

200 previous estimates (1.11 m yr^{-1} °C^{-1}, Reese et al., 2023), whereas that of PICO agrees with the lower bound of this estimate (0.7 m yr^{-1} °C^{-1}).

Qualitatively, all models agree that the melt sensitivities of presently fast-melting ice shelves are above the Antarctic-wide average. These are the Totten/Moscow University ice shelf and the ice shelves located in the Amundsen Sea. Quantitatively, however, the intermodel spread is very large. For Totten/Moscow University, the sensitivities of the Quadratic paramaterisation,

205 the Plume, and LADDIE are approximately a factor 5 to 6 (linear) or 3 to 4 (quadratic) higher than those of PICO and the Neural Network. For the Crosson–Dotson, Thwaites, and Pine Island ice shelves in the Amundsen Sea, the melt sensitivities of the Quadratic parameterisation and LADDIE are approximately a factor 3 higher than those of the other three models (PICO, Plume, and Neural Network). The high sensitivities of Quadratic and LADDIE agree best with previous estimates though (10.8–19.9 m yr^{-1} °C^{-1}, Reese et al., 2023), indicating that the melt sensitivity in the Amundsen Sea may be understimated

210 by the latter three models. More generally, the melt sensitivity of these presently fast-melting ice shelves is most dependent on the choice of the basal melt model.

The deep amplification of melt sensitivities shows a particularly large intermodel spread which exceeds the spread between individual ice shelves (Fig. 3e-f). The Quadratic parameterisation gives the highest values with amplifications above a factor 5 for 30 out of 40 ice shelves. Similar to the deep amplification in reference melt rates, this high amplification can be attributed

215 to the strong depth- and slope-dependence and the omission of meltwater advection. PICO provides deep amplifications at the lower end, with a negligible amplification (values near 1) for most ice shelves with the notable exceptions being Filchner–Ronne and Ross. These low amplifications of PICO result from the relatively uniform melt patterns and melt sensitivities. The deep amplification of the Plume is lowest, with a majority of ice shelves giving a suppression of the melt sensitivity (values below 1) at depth. Finally, LADDIE and the Neural Network show a relatively good agreement in deep amplifications for most

220 ice shelves, with mid-range values around 2 – 5 for most ice shelves. The Neural Network, however, gives a melt suppression at some individual ice shelves, which may be related to the fact that deep, shallow and narrow cavities and channels may not be resolved well in NEMO and therefore have been absent from the training dataset.

The large intermodel spread in both melt sensitivities and deep amplifications combine into extreme differences in terms of melt sensitivities in the deep regions. For example, the linear melt sensitivity in the deepest 10% of the Pine Island ice

225 shelf ranges from 1.3 m yr °C^{-1} (PICO) to 81 m yr °C^{-1} (Quadratic). For Totten/Moscow University, this deep sensitivity ranges from 0.3 m yr °C^{-1} (Neural Network) to 50 m yr °C^{-1} (Quadratic). We identify this intermodel spread in deep melt sensitivities, which can exceed two orders of magnitude in presently fast-melting ice shelves, as the most critical source of model uncertainty in basal melt forcing. Reducing this intermodel spread may be an unavoidable task to reduce uncertainties in future projections of ice sheet mass loss and sea-level rise.

230 ## 4 Conclusions

For five basal melt models of varying complexity, an idealised sub-thermocline 1 °C warming scenario induces an increase by 67 to 240% in Antarctic-wide basal melting, depending on the model, with a median increase of 175%. This large intermodel

spread highlights the challenge to reduce uncertainties induced by basal melt in projections of Antarctic ice mass loss. We calibrated the five models to simulate a common reference state, resulting in comparable average melt rates for present-like

235   conditions. However, already in these reference conditions, different model assumptions lead to large differences in the melt patterns. The intermodel disagreement is enhanced in the melt sensitivities to ocean warming, both for patterns and integrated metrics. Hence, a consistent calibration on present-day melt rates is no guarantee for a consistency in melt sensitivities. The intermodel disagreement applies in particular to melt sensitivities of individual ice shelves and their spatial patterns.

Within the assessed ensemble of five basal melt models, the Quadratic parameterisation has the highest melt sensitivity and

240   the strongest melt enhancement in the deeper regions. PICO displays an overall moderate melt sensitivity which is particularly uniform within each ice shelf. The Plume model has an intermediate average melt sensitivity, which is suppressed (below-average) at depth for most ice shelves. LADDIE has an intermediate melt sensitivity and an intermediate enhancement at depth. Finally, the Neural Network has the lowest melt sensitivity with an intermediate enhancement at depth.

Our results can provide context to interpret more carefully simulations by ice-sheet models using one of these basal melt

245   models. Each model has its advantages and disadvantages in terms of its ease of use, its ability to represent present-day melt patterns, and its potential realism of melt sensitivities to ocean warming. Hence, the models could not be ranked in terms of overall quality, despite the large intermodel spread. Rather, these results can provide guidance for further development of the models or alternative calibration approaches. Moreover, we conclude that future ensemble-based studies – such as the next phase of the Ice-Sheet Model Intercomparison Project (ISMIP7) – should retain a diversity in their basal melt forcing to prevent

250   underestimating uncertainties.

References

Berends, C. J., Stap, L. B., and Wal, R. S. W. v. d.: Strong impact of sub-shelf melt parameterisation on ice-sheet retreat in idealised and
265   realistic Antarctic topography, Journal of Glaciology, pp. 1–15, https://doi.org/10.1017/jog.2023.33, publisher: Cambridge University
Press, 2023.

Burgard, C., Jourdain, N. C., Reese, R., Jenkins, A., and Mathiot, P.: An assessment of basal melt parameterisations for Antarctic ice shelves,
The Cryosphere, 16, 4931–4975, https://doi.org/10.5194/tc-16-4931-2022, publisher: Copernicus GmbH, 2022.

Burgard, C., Jourdain, N. C., Mathiot, P., Smith, R. S., Schäfer, R., Caillet, J., Finn, T. S., and Johnson, J. E.: Emulating Present and Future
270   Simulations of Melt Rates at the Base of Antarctic Ice Shelves With Neural Networks, Journal of Advances in Modeling Earth Systems,
15, e2023MS003 829, https://doi.org/10.1029/2023MS003829, 2023.

Davison, B. J., Hogg, A. E., Gourmelen, N., Jakob, L., Wuite, J., Nagler, T., Greene, C. A., Andreasen, J., and Engdahl, M. E.: Annual mass
budget of Antarctic ice shelves from 1997 to 2021, Science Advances, 9, eadi0186, https://doi.org/10.1126/sciadv.adi0186, publisher:
American Association for the Advancement of Science, 2023.

275 Dutrieux, P., Rydt, J. D., Jenkins, A., Holland, P. R., Ha, H. K., Lee, S. H., Steig, E. J., Ding, Q., Abrahamsen, E. P., and Schröder, M.: Strong
Sensitivity of Pine Island Ice-Shelf Melting to Climatic Variability, Science, 343, 174–178, https://doi.org/10.1126/science.1244341, 2014.

Jourdain, N. C., Asay-Davis, X., Hattermann, T., Straneo, F., Seroussi, H., Little, C. M., and Nowicki, S.: A protocol for calculating basal
melt rates in the ISMIP6 Antarctic ice sheet projections, The Cryosphere, 14, 3111–3134, https://doi.org/10.5194/tc-14-3111-2020, 2020.

Lambert, E., Jüling, A., van de Wal, R. S. W., and Holland, P. R.: Modelling Antarctic ice shelf basal melt patterns using the one-layer Antarc-
280   tic model for dynamical downscaling of ice–ocean exchanges (LADDIE v1.0), The Cryosphere, 17, 3203–3228, https://doi.org/10.5194/tc-
17-3203-2023, publisher: Copernicus GmbH, 2023.

Lazeroms, W. M. J., Jenkins, A., Gudmundsson, G. H., and van de Wal, R. S. W.: Modelling present-day basal melt rates for Antarctic ice
shelves using a parametrization of buoyant meltwater plumes, The Cryosphere, 12, 49–70, https://doi.org/https://doi.org/10.5194/tc-12-
49-2018, 2018.

285 Levermann, A., Winkelmann, R., Albrecht, T., Goelzer, H., Golledge, N. R., Greve, R., Huybrechts, P., Jordan, J., Leguy, G., Martin, D.,
Morlighem, M., Pattyn, F., Pollard, D., Quiquet, A., Rodehacke, C., Seroussi, H., Sutter, J., Zhang, T., Van Breedam, J., Calov, R.,
DeConto, R., Dumas, C., Garbe, J., Gudmundsson, G. H., Hoffman, M. J., Humbert, A., Kleiner, T., Lipscomb, W. H., Meinshausen, M.,
Ng, E., Nowicki, S. M. J., Perego, M., Price, S. F., Saito, F., Schlegel, N.-J., Sun, S., and van de Wal, R. S. W.: Projecting Antarctica's
contribution to future sea level rise from basal ice shelf melt using linear response functions of 16 ice sheet models (LARMIP-2), Earth
290   System Dynamics, 11, 35–76, https://doi.org/https://doi.org/10.5194/esd-11-35-2020, 2020.

Mathiot, P. and Jourdain, N. C.: Southern Ocean warming and Antarctic ice shelf melting in conditions plausible by late 23rd century in a
high-end scenario, Ocean Science, 19, 1595–1615, https://doi.org/10.5194/os-19-1595-2023, publisher: Copernicus GmbH, 2023.

Morlighem, M., Rignot, E., Binder, T., Blankenship, D., Drews, R., Eagles, G., Eisen, O., Ferraccioli, F., Forsberg, R., Fretwell, P., Goel,
V., Greenbaum, J. S., Gudmundsson, H., Guo, J., Helm, V., Hofstede, C., Howat, I., Humbert, A., Jokat, W., Karlsson, N. B., Lee, W. S.,
295 Matsuoka, K., Millan, R., Mouginot, J., Paden, J., Pattyn, F., Roberts, J., Rosier, S., Ruppel, A., Seroussi, H., Smith, E. C., Steinhage, D.,
Sun, B., Broeke, M. R. v. d., Ommen, T. D. v., Wessem, M. v., and Young, D. A.: Deep glacial troughs and stabilizing ridges unveiled
beneath the margins of the Antarctic ice sheet, Nature Geoscience, 13, 132–137, https://doi.org/10.1038/s41561-019-0510-8, 2020.

Otosaka, I. N., Shepherd, A., Ivins, E. R., Schlegel, N.-J., Amory, C., van den Broeke, M. R., Horwath, M., Joughin, I., King, M. D., Krinner,
G., Nowicki, S., Payne, A. J., Rignot, E., Scambos, T., Simon, K. M., Smith, B. E., Sørensen, L. S., Velicogna, I., Whitehouse, P. L., A,

300   G., Agosta, C., Ahlstrøm, A. P., Blazquez, A., Colgan, W., Engdahl, M. E., Fettweis, X., Forsberg, R., Gallée, H., Gardner, A., Gilbert, L.,
       Gourmelen, N., Groh, A., Gunter, B. C., Harig, C., Helm, V., Khan, S. A., Kittel, C., Konrad, H., Langen, P. L., Lecavalier, B. S., Liang,
       C.-C., Loomis, B. D., McMillan, M., Melini, D., Mernild, S. H., Mottram, R., Mouginot, J., Nilsson, J., Noël, B., Pattle, M. E., Peltier,
       W. R., Pie, N., Roca, M., Sasgen, I., Save, H. V., Seo, K.-W., Scheuchl, B., Schrama, E. J. O., Schröder, L., Simonsen, S. B., Slater, T.,
       Spada, G., Sutterley, T. C., Vishwakarma, B. D., van Wessem, J. M., Wiese, D., van der Wal, W., and Wouters, B.: Mass balance of the
305   Greenland and Antarctic ice sheets from 1992 to 2020, Earth System Science Data, 15, 1597–1616, https://doi.org/10.5194/essd-15-1597-
       2023, publisher: Copernicus GmbH, 2023.

       Paolo, F. S., Gardner, A. S., Greene, C. A., Nilsson, J., Schodlok, M. P., Schlegel, N.-J., and Fricker, H. A.: Widespread slowdown in thinning
       rates of West Antarctic ice shelves, The Cryosphere, 17, 3409–3433, https://doi.org/10.5194/tc-17-3409-2023, publisher: Copernicus
       GmbH, 2023.

310   Pelle, T., Morlighem, M., and Bondzio, J. H.: Brief communication: PICOP, a new ocean melt parameterization under ice shelves combining
       PICO and a plume model, The Cryosphere, 13, 1043–1049, https://doi.org/10.5194/tc-13-1043-2019, 2019.

       Reese, R., Albrecht, T., Mengel, M., Asay-Davis, X., and Winkelmann, R.: Antarctic sub-shelf melt rates via PICO, The Cryosphere, 12,
       1969–1985, https://doi.org/10.5194/tc-12-1969-2018, 2018.

       Reese, R., Garbe, J., Hill, E. A., Urruty, B., Naughten, K. A., Gagliardini, O., Durand, G., Gillet-Chaulet, F., Gudmundsson, G. H., Chan-
315   dler, D., Langebroek, P. M., and Winkelmann, R.: The stability of present-day Antarctic grounding lines – Part 2: Onset of irreversible
       retreat of Amundsen Sea glaciers under current climate on centennial timescales cannot be excluded, The Cryosphere, 17, 3761–3783,
       https://doi.org/10.5194/tc-17-3761-2023, publisher: Copernicus GmbH, 2023.

       Rignot, E., Mouginot, J., Scheuchl, B., Broeke, M. v. d., Wessem, M. J. v., and Morlighem, M.: Four decades of Antarctic Ice Sheet mass
       balance from 1979–2017, Proceedings of the National Academy of Sciences, 116, 1095–1103, https://doi.org/10.1073/pnas.1812883116,
320   2019.

       Sallée, J.-B., Vignes, L., Minière, A., Steiger, N., Pauthenet, E., Lourenco, A., Speer, K., Lazarevich, P., and Nicholls, K.: Subsur-
       face floats in the Filchner Trough provide first direct under-ice tracks of eddies and circulation on shelf, EGUsphere, pp. 1–27,
       https://doi.org/10.5194/egusphere-2023-2952, publisher: Copernicus GmbH, 2023.

       van der Linden, E. C., Le Bars, D., Lambert, E., and Drijfhout, S.: Antarctic contribution to future sea level from ice shelf basal melt as
325   constrained by ice discharge observations, The Cryosphere, 17, 79–103, https://doi.org/10.5194/tc-17-79-2023, publisher: Copernicus
       GmbH, 2023.